Directly Confirming the $Z_{1/2}$ Center as the Electron Trap in SiC Through Accessing the Nonradiative Recombination

Yuxiang Gu, Lin Shi, Jun-Wei Luo,* Shu-Shen Li, and Lin-Wang Wang*

SiC is an important wide-bandgap semiconductor for high-power electronics and high-temperature applications. Its $Z_{1/2}$ center, recognized as a carrier lifetime killer, has been extensively studied as it is a key issue impeding many applications of SiC. It is well established that the $Z_{1/2}$ center originates from carbon vacancies (V_C), but direct access to the microscopic mechanism underlying its nonradiative recombination process is lacking. Herein, to consolidate such identification, the multiphonon-assisted nonradiative recombination rates of previously proposed different candidates of the $Z_{1/2}$ center are evaluated by performing first-principles calculations. The calculated electron transition cross sections of the V_C ($\sigma_n = 2.5 \times 10^{-15}$cm^2 at the k-site and $\sigma_n = 3.4 \times 10^{-15}$cm^2 at the h-site) are in accordance with the experimental values [from $\sigma_n = 3.0 \times 10^{-15}$cm^2 to $\sigma_n = 1.0 \times 10^{-14}$cm^2] for the $Z_{1/2}$ center. However, all of the other candidates are orders of magnitudes smaller in transition cross sections. This provides further evidence that the carbon vacancy (V_C) is the $Z_{1/2}$ center from the electron transition cross sections. However, it is also found that the hole transition cross sections of the V_C are very small. Various hypotheses are provided to consolidate this fact with the conclusion that $Z_{1/2}$ is the carrier lifetime killer.

1. Introduction

Silicon carbide (SiC), especially the 4H polytype of SiC, has been recognized as a superior alternative to traditional semiconductors for high-voltage, high-temperature, and low-loss electronic devices owing to its good physical and chemical properties.[1] These properties include: 1) a 3.26 eV wide bandgap and sustaining high critical (breakdown) electric field strength; 2) bipolar doping (doped in both n- and p-type), an exceptional feature among wide-bandgap materials; 3) high compatibility with native oxide SiO$_2$; and 4) high value of hardness, chemical inertness, and high thermal conductivity due to the strong Si—C chemical bond. In addition, its high corrosion and radiation resistance render SiC a key refractory/structural material in space and nuclear radiation environments. Recent advances in growth techniques have enabled the synthesis of high-quality single crystals and large-area epitaxial films for SiC.[2] Various types of semiconductor devices have been demonstrated using SiC, including Schottky diodes, junction-gate field-effect transistors (FETs), metal−oxide−semiconductor FETss (MOSFETs), bipolar transistors, thyristors, and light-emitting diodes (LEDs).[3] However, the wide-bandgap feature renders various deep defect levels within the SiC bandgap. The presence of such electrically active point defects in 4H SiC makes it challenging to increase the minority carrier lifetime to exceed ten microseconds, a crucial criterion for achieving high-voltage bipolar devices (>10 kV blocking voltage and low on-state loss). In contrast, these deep defects may become optically addressable defects (i.e., color centers) with long spin coherence times. This gains significant attention for SiC, specifically the 4H polytype, as a promising platform for quantum bits (qubits) in various quantum communication and sensing applications.[4–7]

Deep-level transient spectroscopy (DLTS) shows in epitaxial 4H SiC thin films grown by chemical vapor deposition (CVD) two most common defect levels: the $Z_{1/2}$ level[8–10] at 0.45–0.71 eV below the conduction band minimum (CBM) of 4H-SiC and the EH$_{6/7}$ level at 1.55–1.65 eV below the CBM,[11,12] respectively. Several studies[13–16] have illustrated that there is a strong correlation between the minority carrier lifetime and the concentration of $Z_{1/2}$ centers, thus concluding that $Z_{1/2}$ is responsible for the minority carrier lifetimes in SiC.[13] The $Z_{1/2}$ and EH$_{6/7}$ centers are not only presented in as-grown samples

Y. Gu, J.-W. Luo, S.-S. Li
State key laboratory of superlattices and microstructures
Institute of Semiconductors
Chinese Academy of Sciences
Beijing 100083, China
E-mail: jwluo@semi.ac.cn

Y. Gu, J.-W. Luo, S.-S. Li
Center of Materials Science and Optoelectronics Engineering
University of Chinese Academy of Sciences
Beijing 100049, China

L. Shi
Suzhou Institute of Nano-Tech and Nano-Bionics
Chinese Academy of Sciences
Suzhou 215123, China

L.-W. Wang
Materials Science Division
Lawrence Berkeley National Laboratory
Berkeley, CA 94720, USA
E-mail: lwwang@lbl.gov

ADVANCED
SCIENCE NEWS

www.advancedsciencenews.com

pss

physica status solidi rrl

www.pss-rapid.com

but also presented during the reactive ion etching (RIE) and ion implantation processes in 4H SiC.[17] The experimentally fitted electron cross sections of the $Z_{1/2}$ centers range from 3×10^{-15} to $1 \times 10^{-14} \, cm^2$.[10,13,17–19] Despite the advances for identifying these defect centers from spectroscopy measurements, the atomic identity of these centers remains unknown for a long time. After extensive study, however,[20–30] it is now commonly believed that the carbon vacancy (V_C) is the atomic identity for the $Z_{1/2}$ center. Son and co-workers[15,27,28] identified $Z_{1/2}$ and E6,7edouble acceptor state and the single donor state of the carbon vacancy (V_C), respectively, after combining electron paramagnetic resonance (EPR) and DLTS measurements. This identification is based on the fact that changing the V_C concentration could alter the carrier lifetime from 2.4 to 26 µs.[29,30] Given these experimental advances, it is highly desirable to theoretically calculate the nonradiative recombination processes of the V_C and other defect centers, to corroborate with the experimental finding.

In this article, we theoretically examine the electron and hole capture process for defects: V_C, V_{Si}, N_i-V_{Si}, and V_C-V_{Si}, all have been proposed as the $Z_{1/2}$ center in previous literature.[11,16–31] We first calculate the formation energies and transition levels of these defect candidates. One challenge in previous theoretical studies of the defect levels is that only the predicted transition energies can be compared with experimental data. In the current study, we also calculated the nonradiative recombination cross section to compare with the experiment. The Shockley−Read−Hall (SRH) effect[32,33] and band-to-band Auger recombination are the two major nonradiative recombination processes in semiconductors. The SRH mechanism is usually the dominant one in nondegenerately doped semiconductors. We thus calculated the SRH cross sections of the capture of electrons and holes for different defects in 4H SiC. We found that V_C has an electron capture cross section close to the experimental values for the $Z_{1/2}$ center (in the range from 3×10^{-15} to $1 \times 10^{-14} \, cm^2$[10,13,17–19]), but the remaining defects have at least two orders of magnitude smaller cross sections. This corroborates well with the experimental conclusion that V_c is the identity of $Z_{1/2}$. Our calculation is made possible by our newly developed method to calculate the electron−phonon coupling constants all at once and a new algorithm to calculate all the phonon modes,[34] as implemented in the PWmat code package.

2. Computational Methods

Defect-assisted nonradiative recombination involves capturing an electron from the conduction band (labeled as the initial electronic state i) by a defect (labeled as the final electronic state f) with the probability W_{if}, accompanying a transfer of electronic energy to lattice vibrational energy via electron−phonon coupling. A subsequent capture of a hole from the valence band can annihilate the electron−hole pair, hence the minority carrier. In the following, we describe the method to calculate the cross section of capturing an electron by a defect. The same method is also applicable to hole capturing. For a deep-level defect with a transition level E_t, multiphonon processes[35,36] are critical, as the energies of the multiple phonons are necessarily to supply the required transition energy $\Delta E_{if} = E_C - E_t$. Such multiphonon-

assisted electronic transitions are usually described within the Condon approximation[37] based on the static coupling approach.[38–40] If the occupancies of the phonon modes are n and m respectively for the corresponding initial and final states, $\Psi_{i,n}(r, R)$ and $\Psi_{f,m}(r, R)$, the nonradiative decay probability W_{if} is then given by the Fermi golden rule.[34,41,42]

$$W_{if} = \frac{2\pi}{\hbar} \sum_n \sum_m p(i, n) |V_{in,fm}|^2 \delta(E_{in} - E_{fm}) \tag{1}$$

where $V_{in,fm} = \langle \Psi_{f,m}(r, R) | H | \Psi_{i,n}(r, R) \rangle$ are the off-diagonal matrix elements of the Hamiltonian H and $p(i, n)$ is the probability of the initial vibrational modes n in the given electronic state i.

$$p(i, n) = \frac{\exp(-E_{in}/k_B T)}{\sum_n \exp(-E_{in}/k_B T)} \tag{2}$$

Subsequently, the summations in Equation (1) are thermal dynamic average over the initial phonon states of occupations n and sum over all the final phonon states of occupations m. Under the Frank−Condon approximation, the electron−phonon wave function is approximated by $\Psi_{i,n}(r, R) = \psi_i(r, R)\phi_{i,n}(R)$, where $\psi_i(r, R)$ is the electronic state at nuclear coordinate R, and $\phi_{i,n}(R)$ is the vibrational wave function with phonon occupation n under the electron in state i. In the static coupling approximation, $\psi_i(r, R)$ and $\psi_f(r, R)$ can be replaced, respectively, by $\psi_i(r, R_a)$ and $\psi_f(r, R_a)$ (R_a represents the minimum energy coordinate from which the electronic transition occurs). $V_{in,fm}$ is then rewritten as

$$V_{in,fm} = \sum_k C_{i,f}^k \langle \phi_{f,m}(R) | Q_k | \phi_{i,n}(R) \rangle \tag{3}$$

where $C_{i,f}^k = \left\langle \psi_f(r, R_a) \middle| \frac{\partial H}{\partial Q_k} \middle| \psi_i(r, R_a) \right\rangle$ is the electronic−phonon coupling constant between electronic states i and f induced by the phonon mode Q_k. Inserting Equation (3) into (1), the nonradiative decay probability W_{if} is obtained as

$$W_{if} = \frac{2\pi}{\hbar} \sum_{k_1, k_2} C_{i,f}^{k_1} C_{i,f}^{k_2} A_{i,f}^{k_1, k_2} \tag{4}$$

here $A_{i,f}^{k_1, k_2}$ is a lattice response matrix in the form

$$A_{i,f}^{k_1, k_2} = \sum_n \sum_m p(i, n) \langle \phi_{f,m} | Q_{k_1} | \phi_{i,n} \rangle \langle \phi_{f,m} | Q_{k_2} | \phi_{i,n} \rangle^* \\ \delta(\hbar\omega_{fm} - \hbar\omega_{in} + \Delta E_{if}) \tag{5}$$

Here, ω_{in} and ω_{fm} indicate the multiphonon energies of the n and m phonons in the initial and final electronic states, respectively, and the δ function enforces the energy conservation in Fermi golden rule. Assuming phonon modes in i and f electronic states are the same, the summation in Equation (5) can be conducted analytically under the harmonic approximation, resulting in a closed form of $A_{i,f}^{k_1, k_2}$ expressed in terms of phonon modes, phonon displacement vectors, and the minimum energy atomic configuration difference between states i and f.[34] It turns out that only the diagonal $k_1 = k_2$ term contributes to Equation (4). Thus, the expression can be further simplified as

**ADVANCED
SCIENCE NEWS**

www.advancedsciencenews.com

pssrrl

physica status solidi

www.pss-rapid.com

$$W_{if} = \frac{2\pi}{\hbar} \sum_k |C_{i,f}^k|^2 A_{i,f}^k \qquad (6)$$

ΔE_{if} of Equation (5) is calculated from the charge transition level $E_t(\alpha, q/q')$, which is usually measured from the host valence band maximum (VBM) $E_V(host)$, for a defect α, from charge state q changed to charge state q'. This defect transition level is calculated as

$$E_t(\alpha, q/q') = \frac{\Delta H_f(\alpha, q) - \Delta H_f(\alpha, q')}{q' - q} - E_V(host) \qquad (7)$$

where $\Delta H_f(\alpha, q)$ is the formation energy of the defect α in the charge state q. Taking V_C defect in 4H SiC as an example, following the study by Wei et al.,[43] its formation energy for the charge state q is given by

$$\Delta H_f(V_C, q) = E_{tot}(V_C, q) - E_{tot}(SiC) + [\mu_C + E_{tot}(C)] + q(E_F + E_V(SiC)) \qquad (8)$$

where E_F is the Fermi energy referenced to the VBM of bulk SiC, and μ_C is the chemical potential of the carbon atom referenced to $E_{tot}(C)$, the total energy per atom of the bulk diamond. In the Si-rich limit, the chemical potential of the Si atom is $\mu_{Si} = 0$ (referenced to $E_{tot}(Si)$, the total energy per atom of bulk Si) and $\mu_C = \Delta H_f(SiC)$, whereas, in the C-rich limit, $\mu_C = 0$ and $\mu_{Si} = \Delta H_f(SiC)$. Note that there are two nonequivalent configurations of V_c: the C atom's vacancy at the cubic (k-site) and hexagonal sites (h-site), respectively.

To obtain the nonradiative transition probability, we carry out the first-principles total energy calculations to get the phonon modes of the lattice vibrations, the electron−phonon coupling constants $C_{i,f}^k$, as well as the defect transition level E_t, as implemented in the PWmat code.[44,45] To take into account the possible long-range strain effects due to Jahn−Teller or pseudo-Jahn−Teller distortion of this defect,[46–50] we use a 576-atom supercell comprising $6 \times 6 \times 2$ 4H SiC primary cells containing a single defect as well as the pristine bulk 4H SiC. A 680 eV cutoff for the planewave basis set and a $1 \times 1 \times 1$ Monkhorst−Pack k-point mesh for Brillouin zone integration in all the calculations are adopted to calculate the total energies of the systems. The screened hybrid functional developed by Heyd, Scuseria, and Ernzerhof (HSE)[51,52] mixed with the exchange potential of Perdew, Burke, and Ernzerhof (PBE)[53] with a mixing ratio of 0.25:0.75 is used for total energy and band structure calculations. The norm-conserving pseudopotentials of the SG15 version are used for Si and C.[54] The supercell method with a periodic boundary condition introduces an artificial Coulomb image interaction for a charged defect. Here, we use our recently developed charge-correction method described in the study by Suo et al.[55] to remove this artificial Coulomb interaction energy. By performing calculations based on the above settings, we predict the equilibrium lattice parameters of bulk 4H SiC to be $a = 3.06\,\text{Å}$ and $c = 10.02\,\text{Å}$, which are in good agreement with experimentally measured values ($a = 3.08\,\text{Å}$ and $c = 10.08\,\text{Å}$[56]). The predicted HSE bandgap of the 4H SiC is 3.23 eV, in excellent agreement with the experimental bandgap of 3.26 eV.[1]

3. Results and Discussion

3.1. Comparing the Calculated Nonradiative Recombination Rates with Experimentally Measured $Z_{1/2}$ Values

To compare directly with experimental measurements for non-radiative recombination rates, we have to calculate the electron capture cross section according to $\sigma_n = W_{if} V/v_{th}$, following the first-principles calculation of W_{if}. V is the volume of the supercell used in simulations and $v_{th} = \sqrt{8k_B T/\pi m}$ is the electron thermal velocity with electron mass m. $Z_{1/2}$ center was found to have negative-U properties,[57] which means that it can trap two electrons with the second electron binding more strongly than the first. We thus need to calculate both $(-/0)$ and $(2-/-)$ charge transitions for all investigated defects. In addition, we also calculate the hole capture cross sections σ_p of V_C and V_{Si} defects. **Table 1** summarizes the calculated σ of investigated candidates of V_C, V_{Si}, N_C-V_{Si}, and V_C-V_{Si} in comparison with the experimental data of the $Z_{1/2}$ center.[10,17–19] We find that the electron capture cross sections of both k-site and h-site V_C defects are very close to the experimental data of the $Z_{1/2}$ center in contrast with that of the remaining defects V_{Si}, N_C-V_{Si}, and V_C-V_{Si}, whose electron cross sections are at least two orders of magnitude smaller. Specifically, the predicted electron capture cross sections of the V_C defects for the $(-/0)$ transition are $\sigma_n = 2.5 \times 10^{-15}\,\text{cm}^2$ for its k-site configuration $V_C(k)$ and $\sigma_n = 3.4 \times 10^{-15}\,\text{cm}^2$ for its h-site configuration $V_C(h)$. Experimentally measured data of the $Z_{1/2}$ center for the $(-/0)$ transition is $\sigma_n = 1.0 \times 10^{-14}\,\text{cm}^2$ measured by DLTS in the study by Hemmingsson et al.,[10] $\sigma_n = 3.0 \times 10^{-15}$ or $\sigma_n = 5.0 \times 10^{-15}\,\text{cm}^2$ also measured by DLTS in other studies,[18,19] and $\sigma_n = 4.0 \times 10^{-15}\,\text{cm}^2$ measured by the isothermal capacitance transient spectroscopy (ICTS).[17] Note that these experimental data in the original article were assigned to the $(0/+)$ transition but later were reassigned to the $(-/0)$ transition by Son et al.[16] For the $(2-/-)$ transition, the calculated electron capture cross sections of the k-site and h-site V_C defects are $\sigma_n = 7.6 \times 10^{-18}$ and $8.2 \times 10^{-17}\,\text{cm}^2$, respectively, in reasonable agreement with the experimentally measured data of the $Z_{1/2}$ center: $\sigma_n = 1.4 \times 10^{-16}$ or $6.0 \times 10^{-17}\,\text{cm}^2$ measured by DLTS[10], $\sigma_n = 2.0 \times 10^{-16}$ or 8.1×10^{-17} measured by DLTS[18,19], and $\sigma_n = 5.4 \times 10^{-17}\,\text{cm}^2$ obtained from the ICTS measurement.[17] Also note that these experimental data in the original article were assigned to the $(-/0)$ transition but later were reassigned to the $(2-/-)$ transition by Son et al.[16]

In contrast, the predicted electron cross sections of the V_{Si} defects for the $(-/0)$ transition are $\sigma_n = 2.0 \times 10^{-20}\,\text{cm}^2$ for the k-site configuration and $\sigma_n = 3.0 \times 10^{-20}\,\text{cm}^2$ for the h-site configuration. For the $(2-/-)$ transition, the calculated electron capture cross sections of the k-site and h-site V_{Si} defects are $\sigma_n = 3.3 \times 10^{-20}$ and $\sigma_n = 1.1 \times 10^{-20}\,\text{cm}^2$, respectively. The predicted values of the V_C-V_{Si} defects for the $(-/0)$ transition are $\sigma_n = 6.2 \times 10^{-17}\,\text{cm}^2$ for the kk-configuration (where kk stands for both V_C and V_{Si} occurred at the k-site) and $\sigma_n = 2.9 \times 10^{-17}\,\text{cm}^2$ for the hh-configuration, and σ_n of the N_C-V_{Si} defects for the $(-/0)$ transition is in a wide range from 1.6×10^{-17} to $9.2 \times 10^{-21}\,\text{cm}^2$. The several orders of magnitude

**ADVANCED
SCIENCE NEWS**
www.advancedsciencenews.com

**physica pss rrl
status
solidi**
www.pss-rapid.com

Table 1. The capture cross sections of different defects in 4 H SiC at temperature $T = 300$ K. The corresponding value of the $Z_{1/2}$ center is determined by DLTS[10,18,19] and ICTS[17] for V_C and V_{Si}, the h or k in the parenthesis stands for a void of atom occurred at the h-site or k-site, respectively. for N_C-V_{Si} complex, the labels in the parenthesis stand for N_C and V_{Si} at h- or k-site, respectively.

|	Defect	$\sigma_n(-/0)$ [cm²]	$\sigma_n(2-/-)$ [cm²]	$\sigma_p(-/0)$ [cm²]	$\sigma_p(2-/-)$ [cm²]
Ab initio calculation	$V_C(k)$	2.5×10^{-15}	7.6×10^{-18}	6.2×10^{-24}	2.0×10^{-21}
	$V_C(h)$	3.4×10^{-15}	8.2×10^{-17}	1.3×10^{-22}	1.0×10^{-19}
	$V_{Si}(k)$	2×10^{-20}	3.3×10^{-20}	2.5×10^{-19}	1.3×10^{-19}
	$V_{Si}(h)$	3.0×10^{-20}	1.1×10^{-20}	2.4×10^{-19}	3.2×10^{-18}
	$V_C-V_{Si}(kk)$	2.9×10^{-17}			
	$V_C-V_{Si}(kk)$	6.2×10^{-17}			
	$N_C-V_{Si}(kk)$	9.2×10^{-21}			
	$N_C-V_{Si}(kh)$	1.6×10^{-17}			
	$N_C-V_{Si}(hk)$	1.0×10^{-18}			
	$N_C-V_{Si}(hh)$	5.7×10^{-19}			
DLTS	Z_1	$> 1.0 \times 10^{-14}$ [10,18,19]	1.4×10^{-16} [10]	5.0×10^{-14} [18,19]	6.5×10^{-14} [18,19]
		3.0×10^{-15}	2.0×10^{-16} [18,19]		
	Z_2	$> 1.0 \times 10^{-14}$ [10]	6.0×10^{-17} [10]	5.0×10^{-14} [18,19]	6.5×10^{-14} [18,19]
		5.0×10^{-15} [18,19]	8.1×10^{-17} [18,19]		
ICTS	Z_1	4.0×10^{-15} [17]	5.4×10^{-17} [17]		

difference between the calculated σ_n of V_{Si}, N_C-V_{Si}, and V_C-V_{Si} defects and the experimentally measured value of the $Z_{1/2}$ render it a relatively good agreement between the calculated V_C value and the measured $Z_{1/2}$ value. This once again confirms that V_c is the atomic structure for the $Z_{1/2}$ center.

To analyze these results further, we next turn to examine the temperature dependence of σ_n. **Figure 1**a shows that, for the $(-/0)$ transition, all defects exhibit exponential growth in $\sigma_n(-/0)$ value with rising temperature. This temperature-dependent enhancement of σ_n arises from the increase in high-energy optical phonon-mode populations. Such temperature dependence yields an order of magnitude enhancement of σ_n for all defects at high temperature. However, V_{Si}, N_C-V_{Si}, and V_C-V_{Si} defects, even at high temperatures (say 1000 K), still have much smaller σ_n than those of the $Z_{1/2}$ centers measured at room temperature.[10,17–19] Suchhuge differences further exclude them as the candidate for the $Z_{1/2}$ center. We found that $\sigma_n(2-/-)$ of the V_C defect has a relatively weak temperature dependence, as

shown in Figure 1b. For instance, $\sigma_n(2-/-)$ increases from 8.2×10^{-17} to 6.2×10^{-16} cm² for V_C when the temperature rises from 300 to 1000 K. This behavior agrees with experimentally measured temperature dependence in electron capture cross sections of the $Z_{1/2}$ centers.[10] The measured electron capture cross section of the $Z_{1/2}$ centers increases less than one order of magnitude from 300 to 1000 K ($\sigma_n = 9.4 \times 10^{-16}\exp(-0.074/kT)[cm^2]$).[17] Such good agreement in the temperature dependence of the electron capture cross sections provides additional evidence for assigning V_c to $Z_{1/2}$.

So far, our calculated electron trapping rate to V_c agrees well with the experimental values through DLTS and ICTS measurements. These are all trapping rates from one type of carrier. To estimate the overall rates of these defects as carrier lifetime killers, one also needs to consider the trapping rates from the opposite carrier: the hole. However, the calculated hole capture cross section of the V_C defect (see Table 1) is rather small. The predicted hole cross sections of the V_C defects for the $(-/0)$
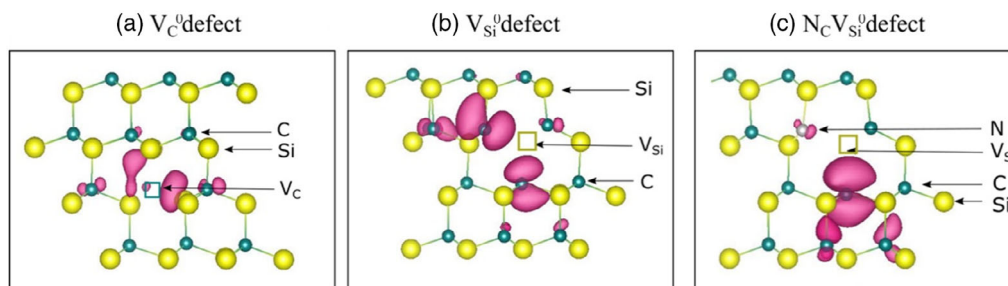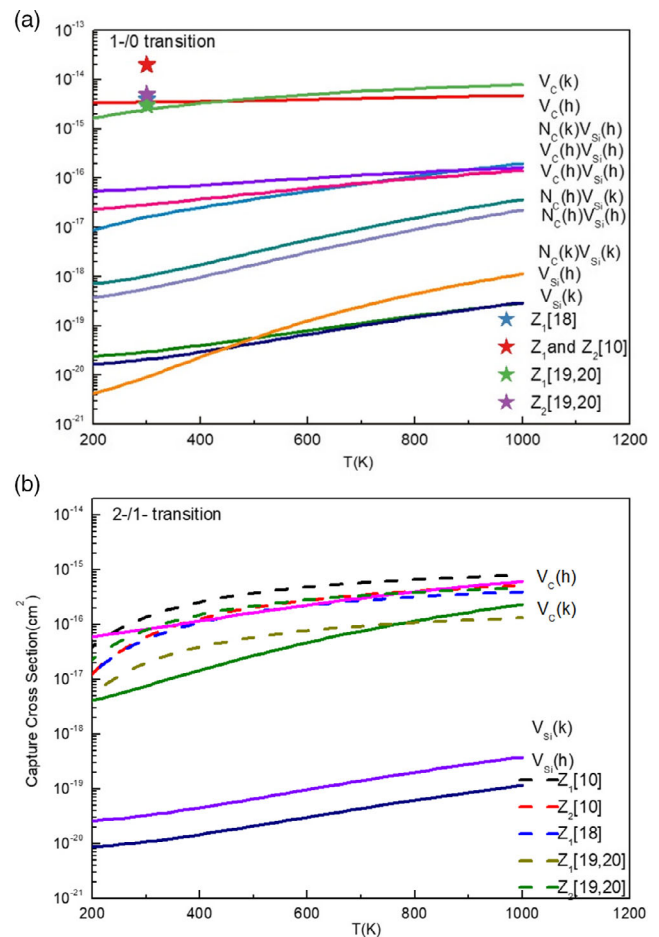

Figure 1. a–c) The atomic structures of $V_C^0(k)$ (a), $V_{Si}^0(k)$ (b), and $N_C-V_{Si}^0(kk)$ (c) defects in 4H-SiC. The purple isosurface in each panel represents charge density corresponding to the defect states.

transition are $\sigma_p = 6.2 \times 10^{-24}$ cm^2 for the k-site configuration and $\sigma_p = 1.3 \times 10^{-22}$ cm^2 for the h-site configuration. For the (2−/−) transition, the calculated electron capture cross sections of the k-site and h-site V_C defects are $\sigma_p = 2.0 \times 10^{-21}$ and $\sigma_p = 1.0 \times 10^{-19}$ cm^2, respectively. Experimentally measured data of the $Z_{1/2}$ center for the (−/0) transition are $\sigma_p = 5.0 \times 10^{-14}$ and $\sigma_p = 6.5 \times 10^{-14}$ cm^2 for the (2−/−) transition measured by DLTS[18,19]. The predicted σ_p of V_C defects are at least five orders of magnitude smaller than the experimental data of the $Z_{1/2}$ center. For SRH recombination, if the defect level is close to the CBM, electrons can be easily trapped but holes can be hard to be captured.[41] As the $Z_{1/2}$ level is at 0.45−0.71 eV below the CBM E_C[8–10] or 2.55−2.81 eV above the VBM E_V, the nonradiative rate of the hole capture is unlikely to be very large. This provides a dilemma to be further studied in the future. One possibility is that the V_C^0 has a C$_{3V}$ symmetry in 4H SiC. After it traps one electron and becomes a 1-state, the symmetry of the system reduces from C$_{3V}$ to C$_{1h}$.[49] The V_C^- defect may undergo a large lattice relaxation to form a negative-U system and get a lower transition level for hole capture. As a result, electron trapping may occur by jumping from the C$_{3V}$ V_C^0 state to the C$_{3V}$ V_C^- state. However, hole trapping may occur by jumping from the C$_{1h}$ V_C^- state to the C$_{1h}$ V_C^0 state with a transition level closer to the valence band. This is a two-level recombination process mentioned in the study by Yang et al.[58] Another possibility is that, the negative charge in V_c^{-2} might attract the hole near the defect state, forming a relatively deep hydrogen-like state (due to the small dielectric constant and large hole effective mass). Such a hydrogen-like state will enhance the hole capture rate in two ways. First, the hole wave function will be more localized near the defect, thus enhancing the phonon-induced coupling to the defect state. Second, the hole energy level will be higher (e.g., around 0.4 eV or even higher), which reduces the transition energy difference, which usually has a major influence on the transition rate. However, to yield a more quantitative result, much more careful calculations have to be carried out in the future.

Figure 2. a,b) First-principles-calculated electron capture cross sections as a function of temperature for different defects for (−/0) transition (a) and for (2−/1−) transition (b). The experimental data are measured by DLTS adopted from other studies[10,18,19] and by ICTS from the study by Kimoto et al.,[17] respectively. Because experimental data are obtained assuming a temperature-independent capture cross section through a fitting, we cite them with room temperature ($T = 300$ K).

3.2. Transition Levels of the Different Defect Centers

Comparing the transition levels between the first-principles calculations and experimental measurements for defect centers has been extensively studied before and has often been used to identify the atomic structures for the spectroscopy-measured defect levels.[46–50] Here, we compare our calculated defect levels to the experimentally measured values. **Figure 2**a,b shows the formation energies as a function of the Fermi level for all the defects studied above under Si-rich and C-rich conditions, respectively. They are all calculated with the hybrid HSE functional. Each line in Figure 2a,b represents the smallest formation energy among different charge states for a specific defect as a function of the Fermi level. The line slope is the stable charge state for a given Fermi level, and the kinks indicate the transition from charge state q to charge-state q' with energy positions responsible for the (q/q') transition levels. The $Z_{1/2}$ centers possess the highest

thermal stability[59] and the highest concentration[9] over other defects observed experimentally in as-grown 4H SiC samples. By comparing the formation energies of all candidates for the $Z_{1/2}$ center, we find that V_c has the lowest formation energy and thus should be the most stable defect with the highest concentration among all considered defects. It is especially true for p-type doping, where the Fermi energy is close to the VBM. As expected, the formation energy of V_C defects under Si-rich conditions is smaller than that under the C-rich condition as it expels C out of the system, as shown in Figure 2a,b. We can infer from the formation energy that the concentration of the V_C defects will increase as the growth changes from C-rich condition to Si-rich condition. Such expectation is consistent with experimental measurements[11,12] where the concentration of the $Z_{1/2}$ centers was indeed observed to be higher under the Si-rich condition than that under the C-rich condition. Furthermore, the formation energies of the V_C defects between h-site and k-site

configurations differ only by about 0.2 eV, indicating that at high-temperature synthesis conditions h-site and k-site V_C defects occur with about a 1:1 ratio. This ratio explains that the two $Z_{1/2}$ centers have almost the same concentrations as observed experimentally,[10,11] if we assign the two $Z_{1/2}$ centers, respectively, to h-site and k-site V_C defects.

We summarize the charge transition levels of all defects in **Table 2**. The $(2-/0)$ and $(-/0)$ charge transitions of the $V_C(k)$ configuration occur at 0.82 and 0.29 eV (they are at 0.90 and 0.41 eV for $V_C(h)$ configuration), respectively, below the host CBM $E_C(SiC)$. In Figure 2c, we compare the $(-/0)$ and $(2-/-)$ transition levels between the V_C defects predicted by the first-principles calculations with the $Z_{1/2}$ centers measured experimentally by EPR[16], as well as the ionization energies of the $Z_{1/2}$ centers determined by DLTS.[10] We can see that the calculated $(-/0)$ transition levels are $E_C - 0.29$ eV for $V_C(h)$ and $E_C - 0.41$ eV for $V_C(k)$, which are close to the experimentally measured $(-/0)$ transition levels of the $Z_{1/2}$ centers ($\approx E_C - 0.45$ eV for Z_1 and $\approx E_C - 0.52$ eV for Z_2).[10] The calculated $(2-/0)$ transition levels of the V_C ($\approx E_C - 0.90$ eV for $V_C(h)$ and $\approx E_C - 0.82$ eV for $V_C(k)$) are also close to that of the $Z_{1/2}$ centers obtained experimentally ($\approx E_C - 0.67$ eV for Z_1 and $\approx E_C - 0.71$ eV for Z_2).[10] In striking contrast, the transition levels of V_{Si} and N_C-V_{Si} approach the host VBM $E_V(SiC)$ with remarkable differences from the measured levels of $Z_{1/2}$. Furthermore, in Figure 2d, we compare the $(0/+)$ and $(+/2+)$ transition levels between the V_C defects with the ionization energies of the $EH_{6/7}$ centers determined experimentally by DLTS.[10] $EH_{6/7}$ centers have also been identified as the donor state of the V_C defects.[17,60] We can see that the $(0/+)$ transition levels are $E_C - 1.51$ eV for $V_C(h)$ and $E_C - 1.59$ eV for $V_C(k)$, which are close to the experimentally measured $(-/0)$ transition levels of the $EH_{6/7}$ centers ($\approx E_C - 1.59$ eV for EH_6 and $\approx E_C - 1.66$ eV for EH_7).[60] The $(+/2+)$ transition levels of the V_C ($E_C - 1.01$ eV for $V_C(h)$ and $E_C - 1.23$ eV for $V_C(k)$) are smaller than that of the $EH_{6/7}$ centers obtained experimentally ($\approx E_C - 1.49$ eV for EH_6 and $\approx E_C - 1.48$ eV for EH_7).[60] Notably, the donor level also has negative-U properties, which agree with the DLTS experiment.[60] At this point, we confirm that $V_C(h)$ is the Z_1 center and $V_C(k)$ is the Z_2 center in DLTS, as assigned in the study by Son et al.[16]

3.3. Mechanisms Underlying the Remarkable Difference in Electron Capture Cross Section Among Different Defects

We now like to discuss the mechanisms regulating the nonradiative recombination rates. According to Equation (4), we can decompose the contributions to the transition rate W_{if} from different phonon modes. Their contributions come from two aspects. One is in the electron−phonon coupling C_{if}^k in Equation (4), which induces the coupling of the electrons by the phonon modes. These are called the promoting phonon modes. **Figure 3**d,h,l,p shows the calculated transition rate W_{if} at room temperature as a function of phonon vibrational energy for V_C, V_{Si}, N_C-V_{Si}, and V_C-V_{Si} defects, respectively. We see that most of the coupling to the transition rate W_{if} comes from the high-frequency phonon modes. The corresponding phonon density of states (ph-DOS) of those candidates are also shown in Figure 3a,e,i, m, respectively. We observe spikes in the ph-DOS responsible for localized defect phonon modes, mainly in the host optical phonon mode region. The second contribution of the phonon mode is the need to supply energy for the energy conservation, as captured in the calculation of the matrix A_{if}^k in Equation (5). These phonon modes are called accepting phonon modes. In a classical picture of nonradiative transitions,[61] lattice vibration of the accepting phonon mode supplies enough energy to lift the defect level to intersect with the host conduction band. In the following sections, we will analyze these two contributions in more detail.

3.3.1. The Effects of Electronphonon−Coupling

Considering that the cross section of the transition is proportional to the square of electron−phonon coupling matrix elements C_{if}^k, we further examine the magnitude of C_{if}^k as a function of phonon vibrational energy for V_C, V_{Si}, N_C-V_{Si}, and V_C-V_{Si} defects, as shown in Figure 3b,f,j,n. First, we see remarkable different behaviors between the single-vacancy defects V_C and V_{Si} and defect complex of N_C-V_{Si}. The defect complex N_C-V_{Si} has more phonon modes involved in the coupling constant C_{if}^k, including both optical phonon and acoustic phonon branches. In contrast, there are fewer phonon modes involved

Table 2. First-principles calculated transition levels of proposed defect candidates for observed $Z_{1/2}$ center in the DLTS spectra. Energy levels are units in eV relative to E_V, the VBM of SiC unless noted elsewhere. E_C denotes the CBM of SiC.

Defect	+/2+	0/2+	0/+	−/0	2−/0	2−/−
$V_C(k)$	2.00 (E_C-1.23)	1.82 (E_C-1.41)	1.64 (E_C-1.59)	2.95 (E_C-0.28)	2.42 (E_C-0.81)	1.89 (E_C-1.34)
$V_C(h)$	2.22 (E_C-1.01)	1.97 (E_C-1.26)	1.72 (E_C-1.51)	2.82 (E_C-0.42)	2.34 (E_C-0.89)	1.86 (E_C-1.37)
$V_{Si}(k)$	1.07	0.99	0.91	1.48	1.53	1.58
$V_{Si}(h)$	1.12	1.04	0.96	1.24	1.18	1.12
$V_C-V_{Si}(kk)$			1.42	1.8		
$V_C-V_{Si}(hh)$			1.75	1.93		
$N_C-V_{Si}(kk)$				0.90		
$N_C-V_{Si}(hh)$				0.67		
$N_C-V_{Si}(kh)$				1.08		
$N_C-V_{Si}(hk)$				0.54		
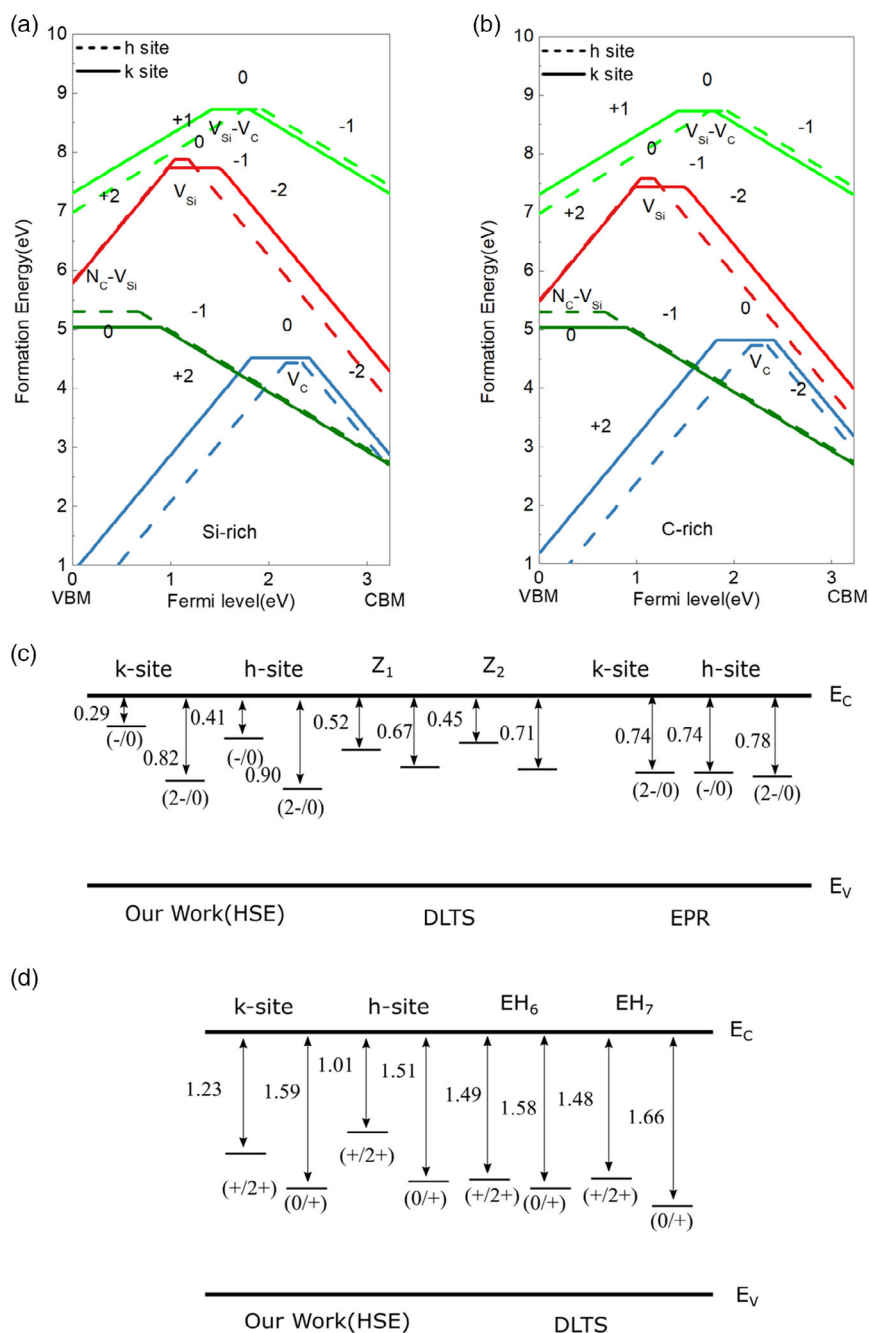
Figure 3. a,b) Formation energy as a function of Fermi level for candidate defects (V_C [blue lines], V_{Si} [red lines], $V_C{-}V_{Si}$ [green lines], and $N_C{-}V_{Si}$ [dark-green lines]) in 4H SiC under Si-rich (a) and C-rich (b) conditions, respectively. The vertical dotted lines represent the energy levels of the $Z_{1/2}$ centers in 4 H SiC observed in DLTS measurements.[10] c) Scheme of acceptor levels of the V_C defects predicted by the first-principles calculations and measured by EPR[16] as well as the $Z_{1/2}$ centers measured by DLTS.[10] d) Scheme of donor levels of the V_C defects predicted by the first-principles calculations as well as the $Z_{1/2}$ centers measured by DLTS.[60]

for the single-vacancy defects, and the strongest coupling comes from the high-frequency optical phonon modes. Note that the many bulk-like phonon modes rather than the localized defect phonon modes make the biggest contribution. We see that C_{if}^k of V_C is one order of magnitude larger than that of V_{Si}. The

difference in C_{if}^k is most likely caused by the difference in wave functions rather than the phonon mode-induced Hamiltonian changes, as V_C and V_{Si} defects share very similar ph-DOSs. As shown in **Figure 4**, the defect wave function in V_C is much more localized than the defect wave function in V_{Si}. Therefore,

**ADVANCED
SCIENCE NEWS**
www.advancedsciencenews.com

pss rrl
physica status solidi
www.pss-rapid.com

we can conclude that the defect level's electronic wave function localization plays an important role in determining the electron−phonon coupling strength.

3.3.2. The Effects of Lattice Relaxation

The energy delta function in A_{if}^k will balance the electronic energy with the lattice vibrational energy to ensure energy conservation in the transition. Thus, energy transition levels of defects determine the number of phonons required to supply the energy for a nonradiative transition. Figure 3c,g,k,o shows A_{if}^k as a function of phonon frequency for different defects. We find that the value of A_{if}^k reduces exponentially with the phonon frequency due to the Bose−Einstein distribution of the phonon population, as shown in Equation (2). This means that the low-frequency phonons might have a higher impact on energy conservations. Figure 3c,g,k,o exhibits that the overall shapes of A_{if}^k as a function of phonon energy are similar among these defects, despite large differences in their overall magnitudes. The

maximum value of A_{if}^k in V_C defect is three orders of magnitude larger than that in V_{Si} defect, four orders of magnitude larger than that in $N_C−V_{Si}$ defect, and two orders of magnitude larger than that in $V_C−V_{Si}$ defect. In addition to phonon energy, the value of A_{if}^k also depends on the amplitude and direction of the minimum energy configuration changes from electron state i to electron state f. At specific phonon energy, the substantial differences in the amplitudes of A_{if}^k between different defects come mostly from their defect-level distances to the conduction band edge. A larger energy difference means more phonons are needed and hence much smaller A_{if}^k. Table 2 indeed shows that the $(−/0)$ transition levels of the V_c defects ($E_C − 0.82$ eV for k-site configuration and $E_C − 0.90$ eV for h-site configuration) are much smaller than that of V_{Si} defects ($E_C − 1.75$ eV for V_{Si} (k) and $E_C − 1.99$ eV for V_{Si} (h)), $N_C−V_{Si}$ defects ($E_C − 2.10$ eV for the hh configuration), and $V_C−V_{Si}$ defects ($E_C − 1.43$ eV for kk-configuration and $E_C − 1.30$ eV for hh configuration).

Finally, we examine the dependences of the electron capture cross section on the defect energy level in **Figure 5**. Although the
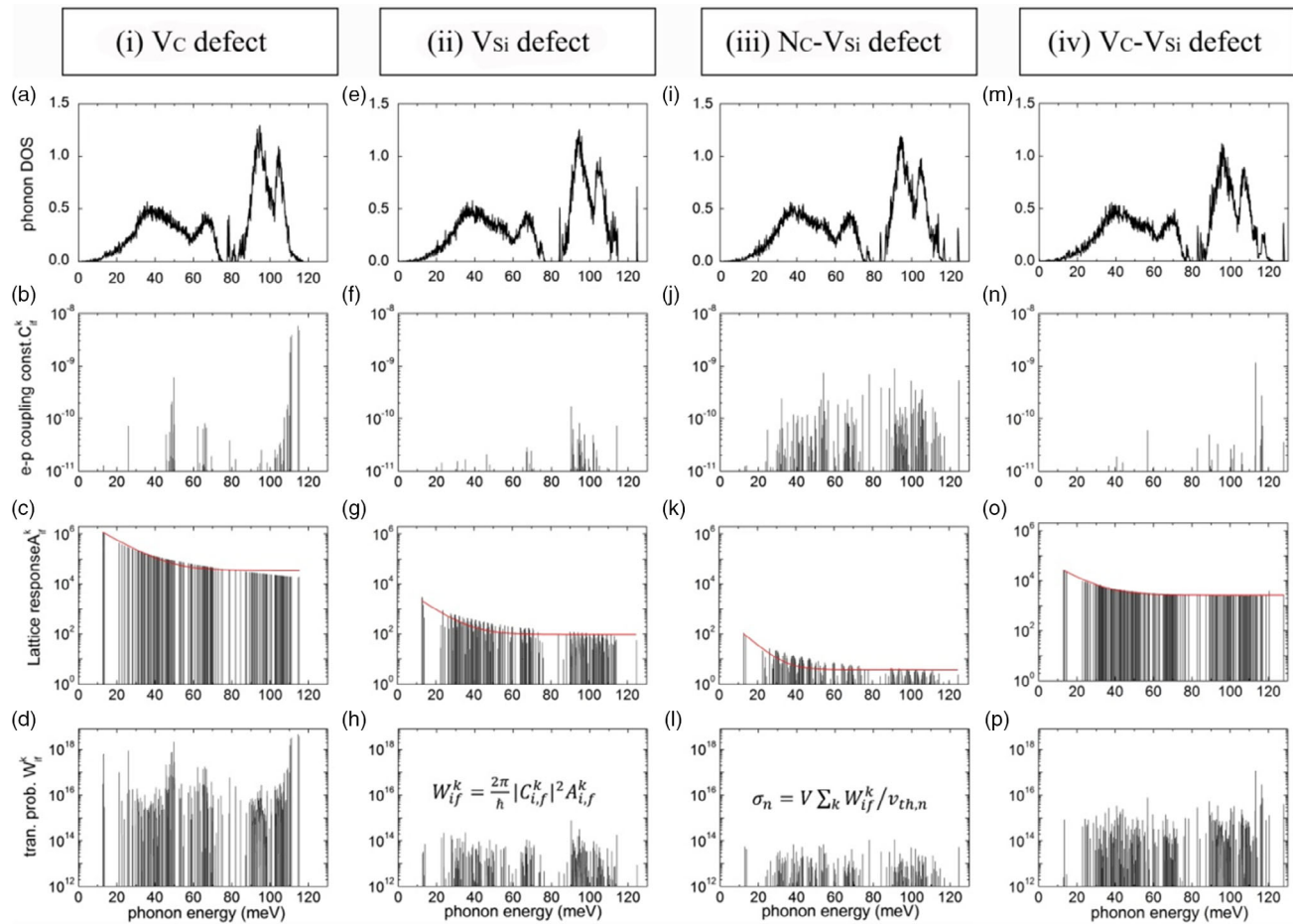
Figure 4. Decomposition of the electron capture cross section into contributions of different phonon modes for V_C (column (i)), V_{Si} (column (ii)), $N_C−V_{Si}$ (column (iii)) defects, and $V_C−V_{Si}$ (column (iv)). Specifically, the ph-DOS for: a) V_C, e) V_{Si}, i) $N_C−V_{Si}$, and m) $V_C−V_{Si}$. The contributions to the electronic matrix element C_{if}^k from different phonon modes, for: b) V_C, f) V_{Si}, j) $N_C−V_{Si}$, and n) $V_C−V_{Si}$. The lattice response component A_{if}^k as a function of phonon frequency, for: c) V_C, g) V_{Si}, k) $N_C−V_{Si}$, and o) $V_C−V_{Si}$. The contributions to the transition rate W_{if} from different phonon modes for: d) V_C, h) V_{Si}, l) $N_C−V_{Si}$, and p) $V_C−V_{Si}$
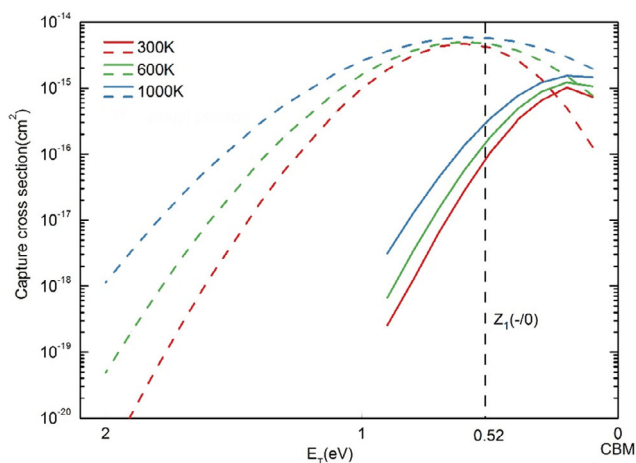
Figure 5. Electron capture cross sections as a function of transition level E_t (measured from SiC CBM) for defects $V_C(k)$ (dashed lines) and $V_{Si}(k)$ (solid lines) at 300, 600, and 1000 K, respectively. The vertical line indicates the experimental data with defect transition levels corresponding to the $Z_1(-/0)$.[10]

transition level of each defect is fixed in real cases, here, we artificially change their energy position alone, while keeping all the other properties intact, to gain insights into the importance of their energy levels. This can also be used to judge, if there is an error in the calculated energy level, how much it can affect the final electron capture cross section. Figure 5 shows the sensitivity of the final nonradiative cross section results as a function of the transition energy. In a high-temperature approximation, the peak position of the cross section as a function of $E_f - E_i$ corresponds to the reorganization energy after the electron transition. This reorganization energy can be written down as $S\hbar\omega$ using the Huang−Rhys' factor S.[62,63] Thus, from the peak positions, we can deduce the reorganization energies for different defects: $S\hbar\omega = 0.6$ eV for the V_C defect, $S\hbar\omega = 0.2$ eV for V_{Si} defect, $S\hbar\omega = 0.4$ eV for $N_C−V_{Si}$ defect, and $S\hbar\omega = 0.4$ eV for $V_C−V_{Si}$ defect. Larger this factor, stronger is the diagonal electron−phonon coupling constant, and softer is the corresponding phonon mode. Considering that the effective phonon energy $\hbar\omega$ should be very similar among these defect as they have the same SiC host lattice, we deduce that the V_C defect has the largest Huang−Rhys' factor S and thus the strongest diagonal electron−phonon coupling constant among all defects considered.

Figure 5 also shows that, for a specific defect, the largest capture cross section occurs if the actual defect transition level E_t is the same as $S\hbar\omega$. We see that, for V_C, E_t is close to $S\hbar\omega$, whereas, for V_{Si} and $N_C−V_{Si}$, their E_t is far away from their $S\hbar\omega$. Therefore, we conclude that the energy position of E_t relative to its relaxation energy $S\hbar\omega$ for a specific defect is a predominant factor in determining the nonradiative decay rate.

4. Conclusion

We verify that the $Z_{1/2}$ center is the V_C defects in 4H SiC, by performing the first-principles calculations of multiphonon-

assisted electron capture cross sections for V_C, V_{Si}, $N_C−V_{Si}$, and $V_C−V_{Si}$ defects in 4H SiC. At room temperature, the electron capture cross section of V_C is in good agreement with the experimental data of the $Z_{1/2}$ center. The agreement in the temperature dependence of electron capture cross sections between V_C defect and $Z_{1/2}$ center provides additional evidence to this assignment. The conclusion was further confirmed by comparing the transition levels between the first-principles calculations and experimental measurements. All these confirm the previous assignment of V_c defects to $Z_{1/2}$ based on experimental correlation between the concentration of V_c and the minority carrier lifetime.[15,27,28] This work also provides an insight into the multiphonon-assisted electron capture processes in terms of different phonon modes. We reveal the mechanisms underlying the dramatic difference in electron capture cross sections among different defects. Specifically, we found that the energy separation of the defect transition levels from the host conduction band is the leading factor in determining the electron capture cross section. The smallest transition level of the V_C defect gives rise to the largest value of the accepting phonon mode factor. Besides the transition level, the localization of the electronic wave function of defect level is also important in determining the promoting electron−phonon coupling constant.

Conflict of Interest

The authors declare no conflict of interest.

Data Availability Statement

Research data are not shared.

[1] T. Kimoto, *Jpn. J. Appl. Phys.* **2015**, *54*, 040103.

[2] Y. Zhang, R. Sachan, O. H. Pakarinen, M. F. Chisholm, P. Liu, H. Xue, W. J. Weber, *Nat. Commun.* **2015**, *6*, 8049.

[3] A. A. Lebedev, *Semiconductors* **1999**, *33*, 107.

[4] W. F. Koehl, B. B. Buckley, F. J. Heremans, C. Greg, D. D. Awschalom, *Nature* **2011**, *479*, 84.

www.advancedsciencenews.com

pss rrl
physica status solidi
www.pss-rapid.com

[5] R. Nagy, M. Niethammer, M. Widmann, Y.-C. Chen, P. Udvarhelyi, C. Bonato, J. U. Hass, an, R. Karhu, I. G. Ivanov, N. T. Son, J. R. Maze, T. Ohshima, Ö. O. Soykal, Á. Gali, S.-Y. Lee, F. Kaiser, J. Wrachtrup, *Nat. Commun.* **2019**, *10*, 1954.

[6] D. M. Lukin, C. Dory, M. A. Guidry, K. Y. Yang, S. D. Mishra, R. Trivedi, M. Radulaski, S. Sun, D. Vercruysse, G. H. Ahn, J. Vučković, *Nat. Photonics* **2020**, *14*, 330.

[7] J. F. Wang, F. F. Yan, Q. Li, H.-H. Liu, J.-M. Cui, Z.-D. Liu, A. Gali, J.-S. Xu, C.-F. Li, G.-C. Guo, *Nat. Commun.* **2021**, *12*, 3223.

[8] T. Dalibor, G. Pensl, T. Kimoto, H. Matsunami, S. Sridhara, R. P. Devaty, W. J. Choyke, *Diamond Relat. Mater.* **1997**, *6*, 1333.

[9] C. G. Hemmingsson, N. T. Son, O. Kordina, J. P. Bergman, J. L. Lindström, S. Savage, N. Nordell, E. Janzén, *J. Appl. Phys.* **1997**, *81*, 6155.

[10] a) C. G. Hemmingsson, N. T. Son, A. Ellison, J. Zhang, E. Janzén, *Phys. Rev. B* **1998**, *58*, R10119; b) C. G. Hemmingsson, N. T. Son, A. Ellison, J. Zhang, E. Janzén, *Phys. Rev. B* **1999**, *59*, 7768.

[11] I. Pintilie, L. Pintilie, K. Irmscher, B. Thomas, *Appl. Phys. Lett.* **2002**, *81*, 4841.

[12] T. Kimoto, S. Nakazawa, K. Hashimoto, H. Matsunami, *Appl. Phys. Lett.* **2001**, *79*, 2761.

[13] P. B. Klein, B. V. Shanabrook, S. W. Huh, A. Y. Polyakov, M. Skowronski, J. J. Sumakeris, M. J. O'Loughlin, *Appl. Phys. Lett.* **2006**, *88*, 052110.

[14] L. Storasta, H. Tsuchida, *Appl. Phys. Lett.* **2007**, *90*, 062116.

[15] T. Hiyoshi, T. Kimoto, *Appl. Phys. Express* **2009**, *2*, 041101.

[16] N. T. Son, X. T. Trinh, L. S. Løvlie, B. G. Svensson, K. Kawahara, J. Suda, T. Kimoto, T. Umeda, J. Isoya, T. Makino, T. Ohshima, E. Janzén, *Phys. Rev. Lett.* **2012**, *109*, 187603.

[17] T. Kimoto, T. Yamamoto, Z. Y. Chen, H. Yano, H. Matsunami, *J. Appl. Phys.* **2001**, *89*, 6105.

[18] I. D. Booker, T. Okuda, J. Hassan, E. Janzén, E. O. Sveinbjörnsson, J. Suda, T. Kimoto, Eur. Conf. on Silicon Carbide and Related Materials 2016 (Halkidiki, Greece, 2016), Tu2a.01.

[19] S. Yamashita, T. Kimoto, *Appl. Phys. Express* **2020**, *13*, 011006.

[20] T. Dalibor, G. Pensl, H. Matsunami, T. Kimoto, W. J. Choyke, A. Schöner, N. Nordell, *Phys. Status Solidi A* **1997**, *162*, 199, and references therein.

[21] T. A. G. Eberlein, R. Jones, P. R. Briddon, *Phys. Rev. Lett.* **2003**, *90*, 225502.

[22] A. Kawasuso, F. Redmann, R. Krause-Rehberg, M. Weidner, T. Frank, G. Pensl, P. Sperr, W. Trifthäuser, H. Itoh, *Appl. Phys. Lett.* **2001**, *79*, 3950.

[23] M. O. Aboelfotoh, J. P. Doyle, *Phys. Rev. B* **1999**, *59*, 10823.

[24] S. Sasaki, K. Kawahara, G. Feng, G. Alfieri, T. Kimoto, *J. Appl. Phys.* **2011**, *109*, 013705.

[25] X. D. Chen, C. L. Yang, M. Gong, W. K. Ge, S. Fung, C. D. Beling, J. N. Wang, M. K. Lui, C. C. Ling, *Phys. Rev. Lett.* **2004**, *92*, 125504.

[26] A. Koizumi, V. P. Markevich, N. Iwamoto, S. Sasaki, T. Ohshima, K. Kojima, T. Kimoto, K. Uchida, S. Nozaki, B. Hamilton, A. R. Peaker, *Appl. Phys. Lett.* **2013**, *102*, 032104.

[27] K. Kawahara, X. T. Trinh, N. T. Son, E. Janzen, J. Suda, T. Kimoto, *Appl. Phys. Lett.* **2013**, *102*, 112106.

[28] K. Kawahara, X. T. Trinh, N. T. Son, E. Janzen, J. Suda, T. Kimoto, *J. Appl. Phys.* **2014**, *115*, 143705.

[29] Eiji Saito, Jun Suda, Tsunenobu Kimoto, *Appl. Phys. Express* **2016**, *9*, 061303.

[30] H. M. Ayedh, R. Nipoti, A. Hallén, B. G. Svensson, *J. Appl. Phys.* **2017**, *122*, 023701.

[31] K. Kanegae, M. Okuda, M. Horita, J. Suda, T. Kimoto, *J. Appl. Phys.* **2021**, *130*, 105703.

[32] W. Shockley, W. T. Read, *Phys. Rev.* **1952**, *87*, 835.

[33] R. N. Hall, *Phys. Rev.* **1952**, *87*, 387.

[34] L. Shi, K. Xu, L. W. Wang, *Phys. Rev. B* **2015**, *91*, 205315.

[35] K. Huang, *J. Semicond* **2019**, *40*, 090102.

[36] C. H. Henry, D. V. Lang, *Phys. Rev. B.* **1977**, *15*, 989.

[37] E. U. Condon, *Am. J. Phys.* **1947**, *15*, 365.

[38] G. Helmis, *Ann. Phys.* **1956**, *19*, 41.

[39] R. Passler, *Czech J. Phys.* **1974**, *24*, 322.

[40] R. Passler, *Czech J. Phys.* **1982**, *32*, 846.

[41] L. Shi, L. W. Wang, *Phys. Rev. Lett.* **2012**, *109*, 245501.

[42] L. W. Wang, *J. Semicond.* **2019**, *40*, 091101.

[43] S.-H. Wei, *Comput. Mater. Sci.* **2004**, *30*, 337.

[44] W. Jia, Z. Cao, L. Wang, J. Fu, X. Chi, W. Gao, L.-W. Wang, *Comput. Phys. Commun.* **2013**, *184*, 9.

[45] W. Jia, J. Fu, Z. Cao, L. Wang, X. Chi, W. Gao, L.-W. Wang, *J. Comput. Phys.* **2013**, *251*, 102.

[46] A. Zywietz, J. Furthmüller, F. Bechstedt, *Phys. Rev. B.* **1999**, *59*, 15166.

[47] B. Michel, H. Matthias, O. Pankratov, *Phys. Rev. B.* **2003**, *67*, 193102.

[48] T. Umeda, Y. Ishitsuka, J. Isoya, N. T. Son, E. Janzén, N. Morishita, T. Ohshima, H. Itoh, A. Gali, *Phys. Rev. B.* **2005**, *71*, 193202.

[49] X. T. Trinh, K. Szász, T. Hornos, K. Kawahara, J. Suda, T. Kimoto, A. Gali, E. Janzén, N. T. Son, *Phys. Rev. B.* **2013**, *88*, 235209.

[50] J. Coutinho, V. J. B. Torres, K. Demmouche, S. Öberg, *Phys. Rev. B.* **2017**, *96*, 174105.

[51] J. Heyd, G. E. Scuseria, M. Ernzerhof, *J. Chem. Phys.* **2003**, *118*, 8207.

[52] J. Heyd, G. E. Scuseria, M. Ernzerhof, *J. Chem. Phys.* **2006**, *124*, 219906.

[53] J. P. Perdew, K. Burke, M. Ernzerhof, *Phys. Rev. Lett.* **1996**, *77*, 3865.

[54] D. R. Hamann, *Phys. Rev. B* **2013**, *88*, 085117.

[55] Z. J. Suo, J. W. Luo, S. S. Li, L. W. Wang, *Phys. Rev. B* **2020**, *102*, 174110.

[56] M. Stockmeier, R. Müller, S. Sakwe, P. Wellmann, A. Mager, *J. Appl Phys.* **2009**, *105*, 033511.

[57] P. W. Anderson, *Phys. Rev. Lett.* **1975**, *34*, 953.

[58] J.-H. Yang, L. Shi, L. W. Wang, S. H. Wei, *Sci. Rep.* **2016**, *6*, 21712.

[59] L. Storasta, F. H. C. Carlsson, S. G. Sridhara, J. P. Bergman, A. Henry, T. Egilsson, A. Hallén, E. Janzén, *Appl. Phys. Lett.* **2001**, *78*, 46.

[60] I. D. Booker, E. Janzen, N. T. Son, J. Hassan, P. Stenberg, E. O. Sveinbjornsson, *J. Appl. Phys.* **2016**, *119*, 235703.

[61] A. M. Stoneham, *Rep. Prog. Phys.* **1981**, *44*, 1251.

[62] K. Huang, A. Rhys, *Proc. R. Soc. A* **1950**, *204*, 406.

[63] Y. Zhang, *J. Semicond.* **2019**, *40*, 091102.